Controlling the strength of ferromagnetic order in $YBa_2Cu_3O_7/La_{2/3}Ca_{1/3}MnO_3$ multilayers

R. de Andrés Prada,[1,2] R. Gaina [ORCID],[1,3] N. Biškup,[4] M. Varela,[4] J. Stahn,[3] and C. Bernhard [ORCID][1]

[1]*Physics Department and Fribourg Center for Nanomaterials (FriMat), University of Fribourg,*
Chemin du Musée 3, CH-1700 Fribourg, Switzerland
[2]*Department of Physics, Stockholm University, AlbaNova University Center, SE-10691 Stockholm, Sweden*
[3]*Laboratory for Neutron Scattering and Imaging, Paul Scherrer Institut, CH-5232 Villigen, Switzerland*
[4]*Departamento de Física de Materiales & Instituto Pluridisciplinar, Universidad Complutense de Madrid, 28040 Madrid, Spain*

With dc magnetization and polarized neutron reflectometry we studied the ferromagnetic response of $YBa_2Cu_3O_7/La_{2/3}Ca_{1/3}MnO_3$ (YBCO/LCMO) multilayers that are grown with pulsed laser deposition. We found that whereas for certain growth conditions (denoted as A type) the ferromagnetic moment of the LCMO layer is strongly dependent on the structural details of the YBCO layer on which it is deposited, for others (B type) the ferromagnetism of LCMO is much more robust. Both kinds of multilayers are of similar structural quality, but electron energy-loss spectroscopy studies with a scanning transmission electron microscope reveal an enhanced average Mn oxidation state of $+3.5$ for the A-type as opposed to the B-type samples, for which it is close to the nominal value of $+3.33$. The related, additional hole doping of the A-type LCMO layers, which likely originates from La and/or Mn vacancies, can explain their fragile ferromagnetic order, since it places them close to the boundary of the ferromagnetic order at which even weak perturbations can induce an antiferromagnetic or glassy state. On the other hand, we show that the B-type samples allow one to obtain YBCO/LCMO heterostructures with very thick YBCO layers and, yet, strongly ferromagnetic LCMO layers.

I. MOTIVATION AND INTRODUCTION

Multilayers based on combining superconducting and ferromagnetic materials are of considerable interest in terms of fundamental questions related to the competition between these antagonistic orders [1,2], as well as for applications in spintronic quantum devices [3]. Recently, great progress has been made with multilayers from conventional superconductors, such as Nb or Al, and ferromagnets, like Fe, Co, or Permalloy. For example, a spin-triplet superconducting (SC) state with Josephson currents through micrometer-thick ferromagnetic barriers has been demonstrated [4,5]. This raises hopes that devices based on spin-polarized supercurrents can soon be realized and integrated into a "superspintronic" technology [3]. A prerequisite for the realization of such spin-polarized superconducting/ferromagnetic quantum states is the design and precise control of the magnetic order, especially around the interface [6].

The research on corresponding superconductor/ferromagnet multilayers from the oxide-based cuprate high-T_c superconductors and the perovskite manganites is comparably less advanced [7–11]. A major difficulty arises from the complexity of these oxide materials and their extremely versatile electronic and magnetic properties [12–14]. These manganites indeed have a very rich temperature and doping phase diagram with various electronic and magnetic phases that are controlled by competing interactions, such as the double-exchange interaction, which stabilizes a half-metallic, ferromagnetic state, and Jahn-Teller distortions, which lead to insulating states with various magnetic and orbital orders [15,16]. Even minor changes of

the local structure and/or the chemical composition can lead to drastic changes of their electronic and magnetic properties. Thus, it is especially challenging to grow thin films with well-controlled properties. It is indeed well known that the ferromagnetic properties of cuprate/manganite multilayers can be strongly dependent on the choice of the substrate, the growth conditions, or the layer thickness, just to name a few of the relevant factors.

Probably, the most widely studied example are multilayers from $YBa_2Cu_3O_7$ (YBCO), which in the bulk is an optimally hole-doped superconductor with $T_c = 90\,\mathrm{K}$, and $La_{2/3}Ca_{1/3}MnO_3$ (LCMO) or $La_{2/3}Sr_{1/3}MnO_3$ (LSMO), which are half-metallic ferromagnets with bulk values of the Curie temperature of $T^{\mathrm{Curie}} = 270$ and $330\,\mathrm{K}$, respectively, and a saturation magnetic moment of $3.7\,\mu_B/\mathrm{Mn}$ ion [17–22]. It was found that a magnetic proximity effect occurs here at the YBCO/LCMO interface, which leads to a suppression of the ferromagnetic order on the manganite side that is commonly denoted as a "dead layer" [23–25]. Concerning the strength of this suppression and the thickness of this "dead layer," the reports appear to be rather controversial. On the one hand, in superlattices made from YBCO and LCMO layers with small individual layer thicknesses of about 10 nm, it was shown that the "dead layer" can be as thin as a single or two LCMO unit cells. The suppression of the ferromagnetic moment is incomplete here, and there is even a weak ferromagnetic moment induced on the YBCO side [26–29]. The average ferromagnetic moment of the thin LCMO layers can exceed $3\,\mu_B/\mathrm{Mn}$ ion, and the Curie temperature can be as high as 220–230 K [20,30]. On the other hand, for multilayers with much thicker individual YBCO and LCMO or LSMO layers,

a more pronounced "dead layer" with a complete suppression of superconductivity has been observed. Furthermore, it was reported that the thickness of the "dead layer" can have a peculiar temperature dependence and increase anomalously below the superconducting transition of the YBCO layer [31–34].

The mechanism(s) responsible for this "dead-layer" formation is at present only poorly understood. In addition to intrinsic effects such as interfacial strain, a transfer of electrons from LCMO to YBCO, and orbital reconstruction [35,36], possible extrinsic factors are chemical intermixing, the formation of oxygen or cation vacancies, and other kinds of structural disorder and defects. Especially, the origin of the long-ranged proximity effect, which gives rise to a "dead layer" in excess of 10 nm, is mysterious and needs to be investigated in more detail.

In the following, we shed more light on this issue and show that the growth conditions of the LCMO layer are playing an important role in defining the thickness of this "dead layer." Moreover, we find that for less perfect growth conditions the structural properties of the YBCO layer are a critical factor.

II. GROWTH AND EXPERIMENTAL

Multilayers of $YBa_2Cu_3O_7$ (Y), $Y_{0.8}Ca_{0.2}Ba_2Cu_{2.8}Co_{0.2}O_7$ (tY), $La_{2/3}Ca_{1/3}MnO_3$ (LC), and $La_{2/3}Sr_{1/3}MnO_3$ (LS) were grown by means of pulsed laser deposition (PLD) on (0 0 1)-oriented $La_{0.3}Sr_{0.7}Al_{0.65}Ta_{0.35}O_3$ (LSAT) single- crystalline substrates (Crystec). The good matching of the pseudocubic lattice constants of these materials ($a^{LSAT} \approx 0.387$ nm, $a^{tY} \approx 0.386$ nm, $a^{LC} \approx 0.387$ nm, $a^{LS} \approx 0.388$ nm) allows for the deposition of heterostructures [17–20,30]. Regarding YBCO, an orthorhombic coordination emerges in the bulk due to the long-range coherence of the one-dimensional CuO chains along the b-axis direction, with $a \approx 0.381$ nm and $b \approx 0.388$ nm. In thin films, however, the substrate induces a strain in the structure of YBCO that results in an average lattice constant of $a^Y \approx 0.385$ nm. The layer sequence and thicknesses of the heterostructures are in the following denoted according to the growth direction and in units of nanometer, i.e., as Y-15/LC-15 for a bilayer that consists of a 15-nm bottom layer of $YBa_2Cu_3O_7$ and a 15-nm top layer of $La_{2/3}Ca_{1/3}MnO_3$.

For the growth, we used an excimer KrF laser ($\lambda = 248$ nm, $t_s = 25$ ns) with a size of the laser footprint on the target of about 3 mm^2. The deposition was monitored with *in situ* reflection high-energy electron diffraction (RHEED) using a collimated 30-kV electron gun at low incidence angle. The substrates were glued with silver paint on a stainless-steel sample holder. This holder was heated from the back side with an infrared laser, and the temperature was monitored and controlled with an internal pyrometer. Before the deposition, the substrates were heated at a rate of 20 °C min^{-1} to the deposition temperature and maintained at the growth pressure and temperature for a minimum of 60 min before the deposition initiated. After deposition, the samples were cooled at a rate of 10 °C min^{-1}. At 700 °C the oxygen pressure in the chamber was increased to 1 bar, and the cooling rate was increased to 30 °C min^{-1} until the desired *in situ* annealing temperature was reached. Two different sets of growth conditions have been used in the deposition of the several species composing the samples, schematically listed in Table I.

In addition to the *in situ* RHEED monitoring of the growth, the structure and composition of the samples were studied by means of x-ray diffraction (XRD), x-ray reflectivity (XRR), scanning transmission electron microscopy (STEM), and electron energy-loss spectroscopy (EELS). The XRD and XRR measurements were carried out with a commercial Rigaku SmartLab triple-axis diffractometer with a rotating-anode Cu $K\alpha$ source ($\lambda = 1.54$ Å). Both XRR and XRD were performed at room temperature. STEM-EELS measurements were carried out in a JEOL ARM200cF equipped with a spherical aberration corrector and a Gatan Quantum EEL spectrometer operated at 200 kV. The specimens for STEM were prepared down to the [110] orientation by conventional techniques, including mechanical grinding and Ar ion milling.

The magnetic properties of the samples were probed by dc magnetization measurements using a vibrating sample magnetometer (VSM) and by polarized neutron reflectometry (PNR). The VSM data were acquired with a commercial physical properties measurement system by Quantum Design (QD-PPMS) equipped with a VSM motor and a pickup coil. The sample was fixed to a quartz rod and vibrated with a frequency of 40 Hz and peak amplitude of 2 mm. The magnetic field was applied parallel to the surface of the sample. The magnetic moment sensed by the pickup coil is a collective contribution of the sample and the substrate. Accordingly, a diamagnetic plus a weak paramagnetic signal of the LSAT substrate have been subtracted to obtain the magnetization of the sample, m. The latter has been attributed to the Mn ions and in the following is presented in units of μ_B/Mn according to the expression

$$m[\mu_B/Mn] = \frac{m \text{ [emu]}}{\mu_B[\text{J T}^{-1}]} \times 10^{-3}\left[\frac{\text{J}}{\text{T emu}}\right]$$
$$\times \frac{\text{Volume manganite unit cell}}{\text{Volume manganite layers}}.$$

TABLE I. Description of the two different types of PLD growth parameters.

	Set A growth conditions	Set B growth conditions
Deposition temperature	825 °C	840 °C
Deposition pressure	$P_{O_2} = 0.30$ mbar	$P_{O_2} = 0.34$ mbar
Laser fluency	2.00 J/cm^2	1.42 J/cm^2
Laser frequency	2 Hz	7 Hz
Postgrowth	Pressure gradually increased at a constant flow of 200 sccm of O$_2$ while slowly cooling to 700 °C	Growth pressure maintained while slowly cooling to 700 °C
In situ annealing	485 °C for 1h	485 °C for 1h, then 400 °C for 1 h

PNR measurements were performed at the AMOR beamline at the SINQ facility of the Paul Scherrer Institute (PSI) in Villigen, Switzerland. These measurements were performed in time-of-flight mode for a wavelength range of 4–13 Å using the SELENE setup [37,38]. At first, the reflectivity curves were measured in the paramagnetic state at 300 K to determine the nuclear depth profile. No difference in the reflectivity curves for spin-up and spin-down polarization was observed here. Subsequently, the samples were measured at 90 K $\ll$ T^{Curie}, after cooling in a magnetic field of 0.46 T applied along the in-plane direction, with polarized neutrons in spin-up and spin-down configurations. The obtained reflectivity curves were fitted with the program SUPERFIT from the Max Planck Institute in Stuttgart. Note that for the nuclear depth profile, while the quality of the fit is fairly good, we could not find a unique solution, i.e., similarly good fits could be obtained with somewhat different fit parameters. One possible reason is due to the lack of phase information in reflectometry, which means that there is no unique relation between a density profile and the measured reflectivity. It is probably of minor importance here, since additional information on the substrate material, approximate densities, thicknesses, and order of the layers is available. It is probably more important that a rather large number of sublayers with independent thicknesses and densities was used for describing the density profile, which increases the correlation between these parameters. If, in addition, the simulation algorithm does not exactly describe the experimental situation, fitting tends to compensate for these systematic deviations by using the available parameters. In the present case, we assume that the leading systematic variations are that the film might not show homogeneous thickness throughout the surface, and that SUPERFIT does not correctly account for the q dependence of the resolution function of the SELENE setup. Note that the remaining uncertainty in the nuclear depth profile does not strongly affect the fitting of the magnetic depth profile, which is governed by the asymmetry of the spin-up and spin-down curves and thus is less sensitive to the resolution function and probable shortcomings of the structural model.

III. RESULTS AND DISCUSSION

A. X-ray diffraction and reflectometry study

Figure 1 compares the XRD and XRR curves of two LC-15/Y-15 and Y-15/LC-15 bilayers that were both deposited with the A-type growth conditions (see Table I). The only difference between these two bilayers concerns the stacking sequence of the YBCO and LCMO layers. The Θ-2Θ scans in Figs. 1(a) and 1(b) reveal (0 0 l) Bragg peaks that are reasonably strong and narrow, and confirm the epitaxial and c-axis-oriented growth of the layers. No traces of misoriented material or of impurity phases can be found. Figure 1(c) details the region around the LSAT (0 0 1), LCMO (0 0 1), and YBCO (0 0 3) Bragg peaks, which reveal clear satellite oscillations that are characteristic of a high crystalline quality and coherence of the layers. Finally, Figs. 1(d) and 1(e)

	thickness (Å)	roughness (Å)
YBCO	179	36
LCMO	161	3

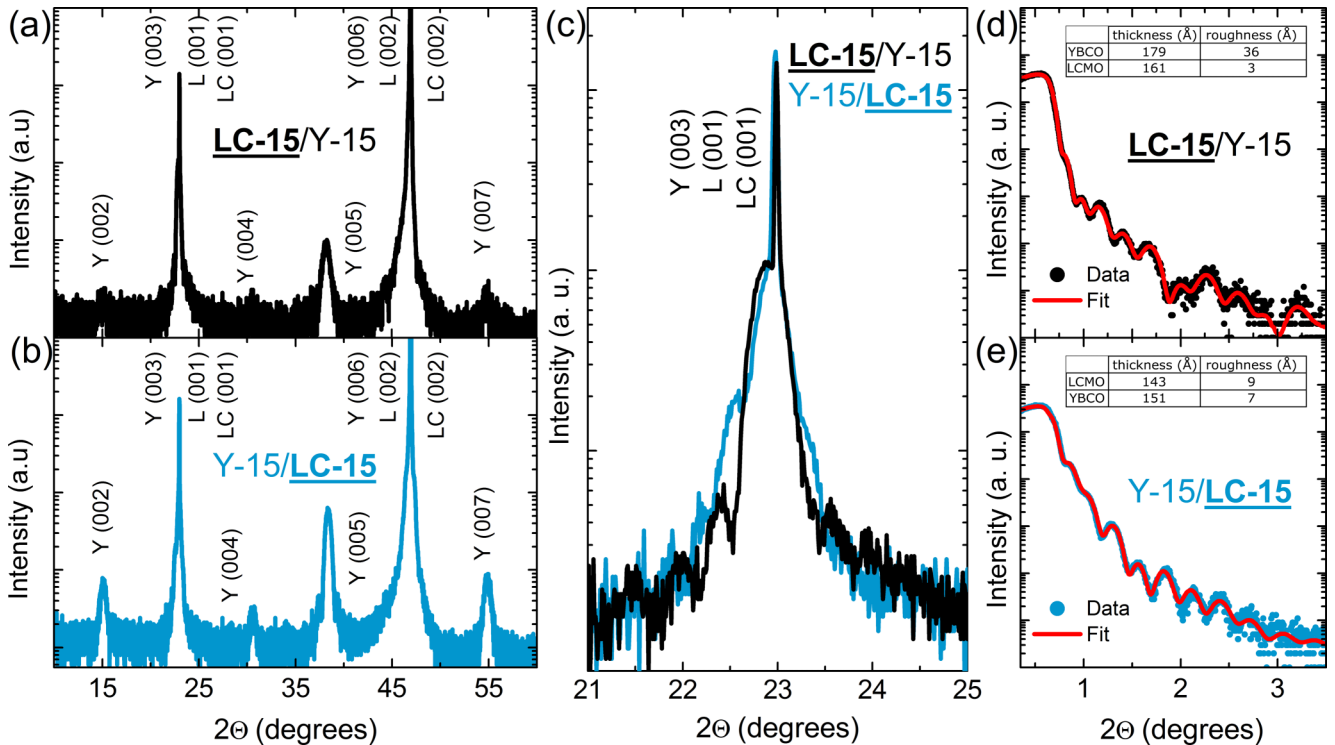|	thickness (Å)	roughness (Å)
LCMO	143	9
YBCO	151	7

FIG. 1. X-ray data of the LC-15/Y-15 (black lines) and Y-15/LC-15 (blue lines) bilayers grown with the A-type conditions described in Table I. (a, b) The Θ-2Θ scans of the LC-15/Y-15 and Y-15/LC-15 bilayers, respectively. (c) Detailed view of the overlapping LSAT (0 0 1), LCMO (0 0 1), and YBCO (0 0 3) Bragg peaks. The presence of satellite oscillations demonstrates the long-range coherence of the crystalline planes. (d, e) X-ray reflectivity (XRR) curves (symbols) with the respective fits (red lines) and the deduced thickness and roughness parameters. The Bragg peaks corresponding to each material are labeled as Y for YBCO, L for LSAT, and LC for LCMO.
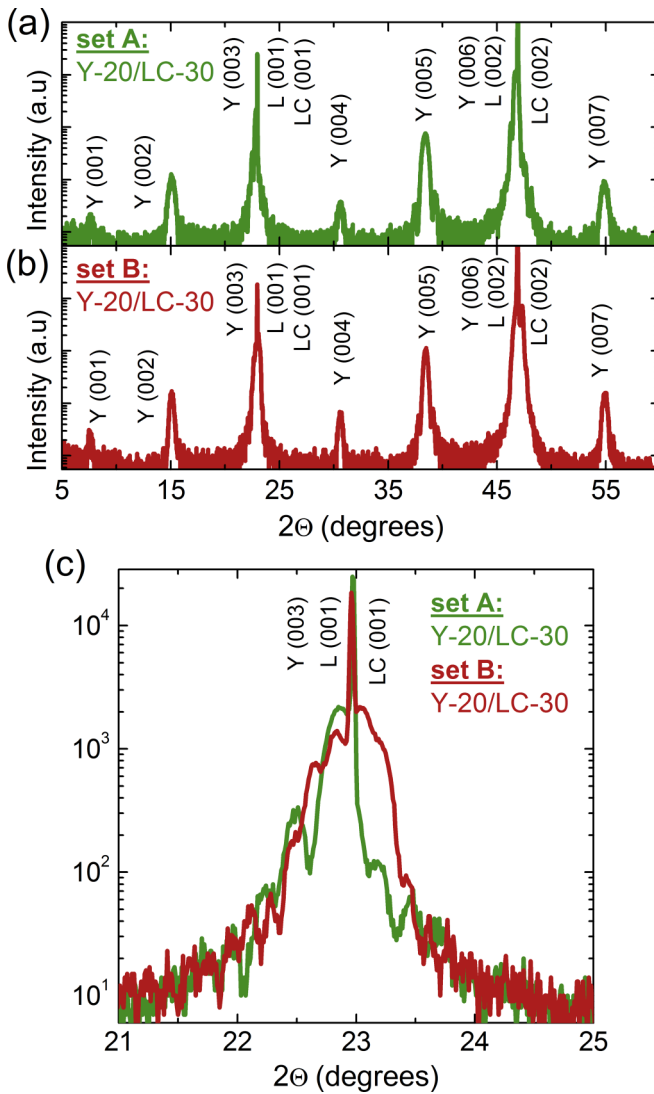
FIG. 2. X-ray data of the Y-20/LC-30 bilayers grown with the A-type (green lines) and B-type (red lines) conditions. (a, b) The Θ-2Θ scans of the type-A and type-B bilayers, respectively. (c) Detailed view of the overlapping LSAT (0 0 1), LCMO (0 0 1), and YBCO (0 0 3) Bragg peaks. Satellite oscillations are observed for both bilayers, which demonstrate a long-range coherence of the crystalline planes. The Bragg peaks corresponding to each material are labeled as Y for YBCO, L for LSAT, and LC for LCMO.

show the XRR curves obtained on each bilayer. Pronounced Kiessig fringes occur for both bilayers, indicating that the interfaces between the different layers are reasonably sharp and coherent. From the fits (red lines) we obtained the thickness and roughness parameters of the layers as listed in the insets.

Next, Fig. 2 compares the XRD curves of two Y-20/LC-30 bilayers that were grown with the different PLD conditions A and B. Figures 2(a) and 2(b) compare the Θ-2Θ scans for the A-type (green) and B-type (red) bilayers, respectively. For both growth types, they confirm a uniform orientation of the films along the *c* crystalline direction, without traces of impurity phases or parts that are misoriented. The closeup of the LCMO (0 0 1) and YBCO (0 0 3) peaks in Fig. 2(c)

reveals that for both the A-type and B-type bilayers there exist similarly pronounced satellite peaks that testify for a comparably high crystalline quality of the YBCO and LCMO layers. The main difference concerns a very small shift of the center of the peak which occurs at a slightly smaller angle for the A-type sample.

B. Scanning transmission electron microscopy

One B-type Y-22/LC-30 bilayer and three A-type Y-15/LC-20, Y-15/LC-15, and Y-10/LC-15/Y-30 structures have been investigated by means of atomic-resolution STEM-EELS techniques. Figures 3 and 4 show representative results for the B-type Y-22/LC-30 and A-type Y-15/LC-20 bilayers for which the most extensive STEM-EELS studies have been performed.

High-resolution STEM high-angle annular dark-field (HAADF) images are compared in Figs. 3(a) and 3(b), showing the YBCO layers for the B-type and A-type case, respectively. A black arrow highlights the position of the LCMO/YBCO interface for both images. The blemished spot in the middle of Fig. 3(a) is an artifact consequence of sample preparation (ion milling) and is not inherent to the as-grown sample. The interfaces appear coherent and mostly defect-free. Both A- and B-type YBCO layers exhibit a number of stacking faults in the form of Y-124-like double or even triple CuO chains (darker horizontal atomic planes) [39,40]. In the case of the A-type sample in Fig. 3(b), these stacking faults are quite evenly distributed throughout the 15-nm-thick YBCO layer. For the thicker B-type YBCO in Fig. 3(a) they are concentrated within the first 14 nm above the substrate, whereas the last seven atomic layers of YBCO, i.e., those close to the LCMO interface, exhibit the expected Y-123 structure. This finding indicates that the formation of these stacking faults and the related nonstoichiometric growth might be enhanced by the strain relaxation of the YBCO layer, which is known to occur within the first 15 nm [30,41].

Figures 3(a)–3(d) reveal that the LCMO layers within both B-type and A-type samples exhibit a good degree of crystallinity. Nevertheless, the analysis of EELS linescans, including the Mn $L_{2,3}$ absorption edge, which was acquired along the out-of-plane direction as indicated by the thick yellow bars in Figs. 3(c) and 3(d), suggests clear differences in the electronic properties of the LCMO layers. Note that the linescan of the B-type sample in Fig. 3(c) does not span the entire 30-nm-thick LCMO layer but tracks the manganese signal (in our case the Mn $L_{2,3}$ white line at an approximate energy loss of 640 eV) only in a range of 10 nm from the YBCO/LCMO interface. The manganese $L_{2,3}$ intensity ratio depends on the oxidation state of manganese ion and can be used for a quantification [40]. The Mn $L_{2,3}$ ratio of the two samples, derived with a double derivative method [42], is plotted in Fig. 3(e). Black squares and red circles denote the B-type and A-type samples, respectively. The right axis shows the corresponding Mn oxidation state based on the calibration of bulk manganite samples. The oxidation state of manganese on the B-type sample across the B-type manganite layer is close to the nominal value of +3.33, as expected for this
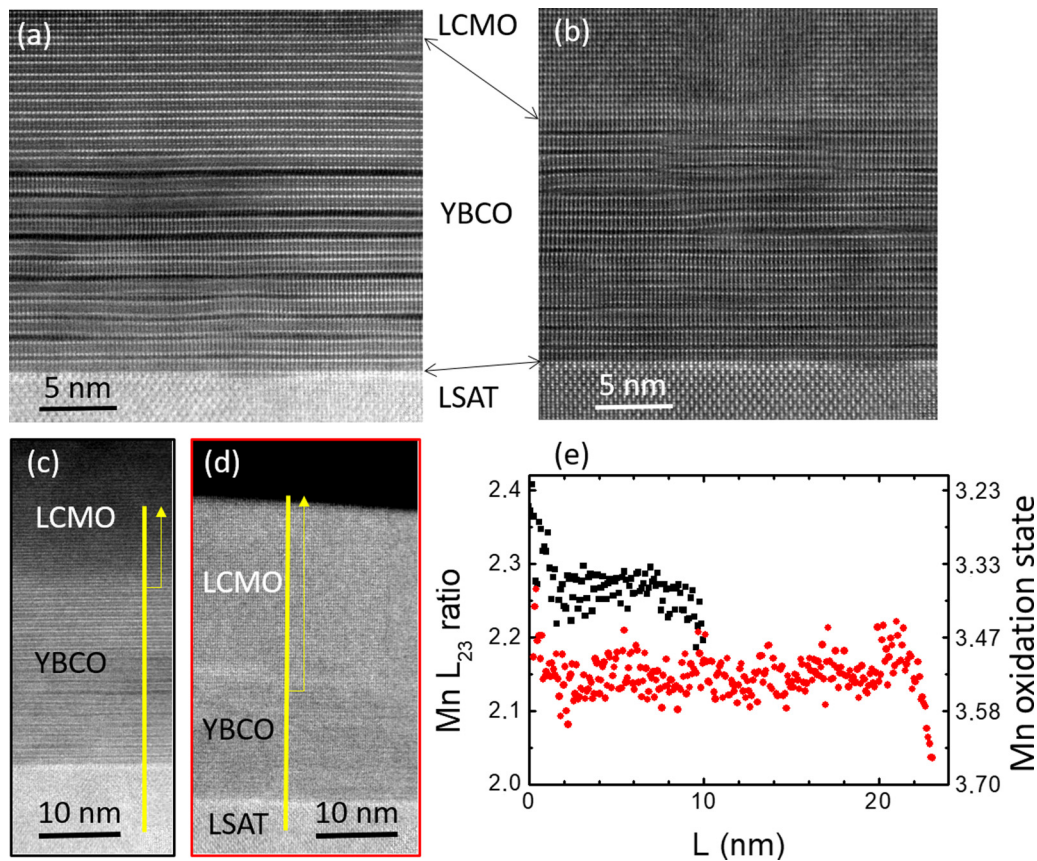
FIG. 3. High-resolution ADF images of (a) a B-type Y-22/LC-30 and (b) an A-type Y-15/LC-20 bilayer, respectively. The LSAT-YBCO and YBCO-LCMO interfaces are marked by arrows. Panels (c) and (d) show the survey images for the EELS linescans across the layers. Panel (e) shows the manganese $L_{2,3}$ ratio across the LCMO layer for the B-type (black squares) and the A-type bilayers (red circles). The position where $L = 0$ nm has been chosen to indicate the location of the LCMO/YBCO interface and the distance L is measured in the direction of the arrows in panels (c) and (d).

compound, while in the A-type sample it has a significantly higher value of about $+3.5$. Note that similarly high values of the manganite oxidation state have been observed for the other two A-type samples. Such an enhanced manganese oxidation state of $+3.5$ suggests the possibility of a nonstoichiometric chemical composition of the A-type $La_{1-x}Ca_xMnO_3$ layers, which would lead to an enhanced hole doping to a level comparable to that of $La_{0.5}Ca_{0.5}MnO_3$, i.e., close to the antiferromagnetic border in the $La_{1-x}Ca_xMnO_3$ phase diagram [15,16]. Since an excess oxygen concentration is typically not observed in these manganese perovskites, the most likely cause is due to the presence of Mn and/or La vacancies [43–47]. If present, Mn vacancies also give rise to disorder effects that can suppress the ferromagnetic order. Note that small amounts of such randomly oriented point defects would not be directly detectable in the STEM experiments. The STEM-EELS probe would be sensitive to local compositional fluctuations of a few percent units at best but would hardly detect small amounts of point defects evenly distributed in a solid solution.

Possible reasons for such a cation deficiency of the manganite layers are scattering effects between the species of the plasma plume or a resputtering of the cations from the surface of the growing film by the highly energetic plasma.

Both effects are expected to be stronger for the A-type growth condition, for which the laser fluency is larger than for the B type, see Table I. The resputtering effect can be further enhanced by the lower substrate temperature of the A-type growth condition, which reduces the diffusion rate of the adatoms prior to their bonding to the thermodynamically stable sites.

Figure 4 shows a number of atomic-resolution EELS images of the LCMO/YBCO interface of the A-type bilayer. The right panel exhibits a high-magnification HAADF image of the interface. A yellow rectangle depicts the region where an EELS spectrum image was taken. The simultaneously acquired annular dark-field (ADF) signal and elemental maps based on the analysis of the O K, Mn $L_{2,3}$, Ba $M_{4,5}$, La $M_{4,5}$, and Cu $L_{2,3}$ edges are shown on the left panels (respectively, from left to right). In spite of some spatial drift, the atomic columns are clearly resolved. The elemental profiles, obtained by horizontal averaging of each two-dimensional elemental map, are shown on the survey ADF image. The atomic plane stacking of the LCMO/YBCO interface can be extracted from these data; it is such that a manganite MnO_2 plane from the LCMO faces a BaO plane from YBCO, as is often observed in this system [28,30,48,49]. Yellow, green, and orange points in the ADF images depict the positions of Ba, La, and Mn
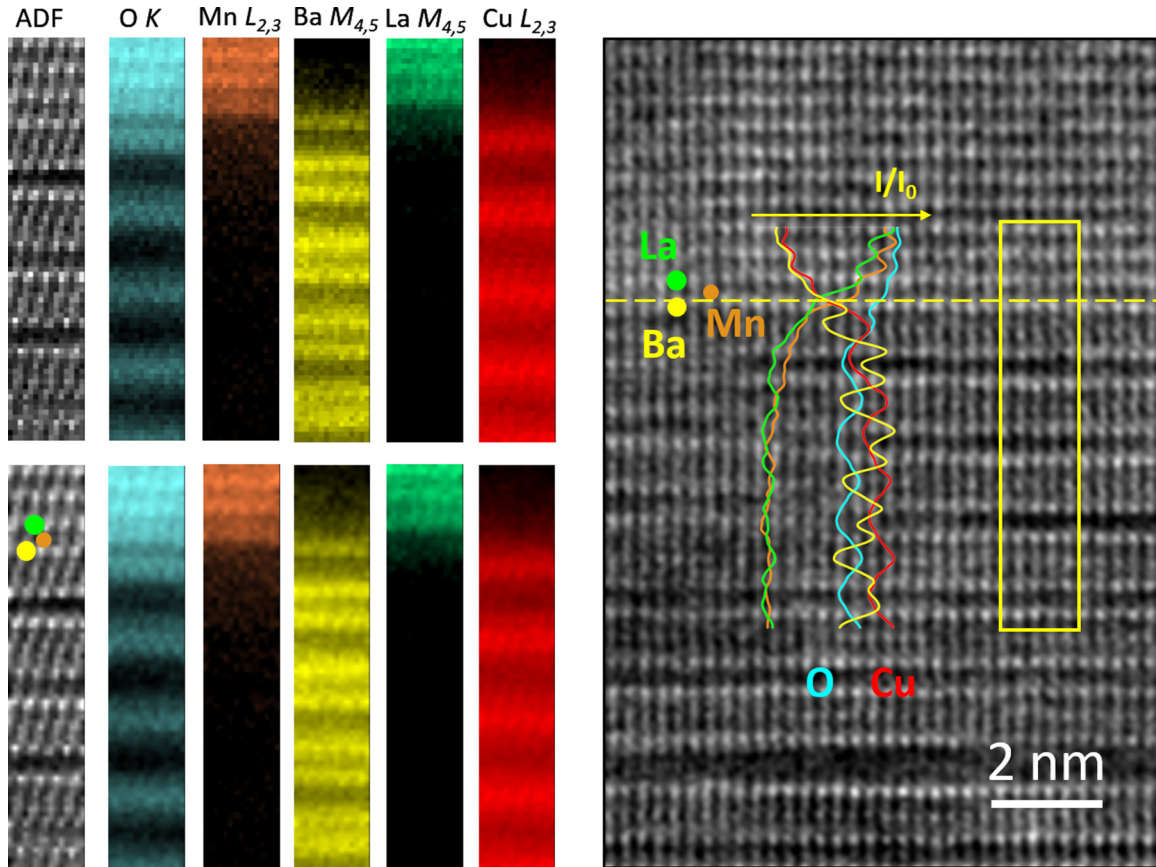
FIG. 4. Right panel: The EELS survey image on the A-type bilayer showing the region where EELS data are acquired (yellow rectangle). The LCMO/YBCO interface is marked by the dashed yellow line, and three particular atoms of La, Mn, and Ba at the interface are indicated by circles. Left panel: The simultaneous ADF image and elemental maps based on the O K, Mn $L_{2,3}$, Ba $M_{4,5}$, La $M_{4,5}$, and Cu $L_{2,3}$ edges (top: raw images, bottom: smoothed data). The inset in the right panel shows the laterally averaged profiles corresponding to these two-dimensional maps, in the same color scale. Random noise in the EELS data was removed by means of principal component analysis.

atoms at the LCMO/YBCO interface. The interface itself is indicated by a yellow dashed line. This type of interface termination has been found in both the A- and B-type samples, although in the former sample a different, $LaO - CuO_2$ termination has also been detected on occasion. This second type of termination is absent for the B-type sample, but we cannot discard its existence due to the lack of statistics of the technique.

Accordingly, the most important difference between the A- and B-type bilayers concerns the average manganese oxidation state, which is close to the nominal one of $+3.33$ for the latter but clearly enhanced to about $+3.5$ for the former case. On the other hand, for both types of bilayers, the LCMO layers are of a comparable structural quality and the YBCO/LCMO interfaces are well defined and atomically sharp with no sign of chemical intermixing. For both bilayers the typical MnO_2-BaO-CuO_2 interlayer stacking sequence dominates, albeit for the A-type bilayer a different, MnO_2-LaO-CuO_2 termination has been detected occasionally. The YBCO layers of the A- and B-type samples contain stacking faults in terms of CuO bilayers that seem to be more abundant in the strain relaxation region within about 15 nm of the LSAT substrate. The limited statistics of the STEM data does not allow us to draw firm conclusions about the differences

between the A- and B-type samples concerning these YBCO stacking faults and the minority interfacial layer stacking sequence.

C. Magnetic properties of LCMO layers

1. DC magnetization of A-type Y-15/LC-15 and LC-15/Y-15 with inverted stacking sequence

Figure 5 shows the magnetization data for the 15/15 bilayers described in Sec. III A. The magnetization curves reveal that the ferromagnetic signal is much stronger for the LC-15/Y-15 bilayer than for the Y-15/LC-15 one. The dc magnetization data in Fig. 5(a), which were taken in field-cooling mode with an external field of $H_{ext} = 1$ kOe applied parallel to the layers, show for LC-15/Y-15 a pronounced ferromagnetic transition around $T^{Curie} \approx 200$ K, with a spontaneous magnetization at 90 K that reaches about 2.75 μ_B/Mn ion. Note that the magnetization data below 90 K are strongly affected by the superconducting response of the YBCO layer and are therefore not further discussed here. In stark contrast, the magnetic signal of the Y-15/LC-15 bilayer shows no clear sign of a ferromagnetic transition and increases only gradually toward low temperature, reaching a value of only 0.12 μ_B/Mn ion at 90 K, which is more than 20 times smaller than that of

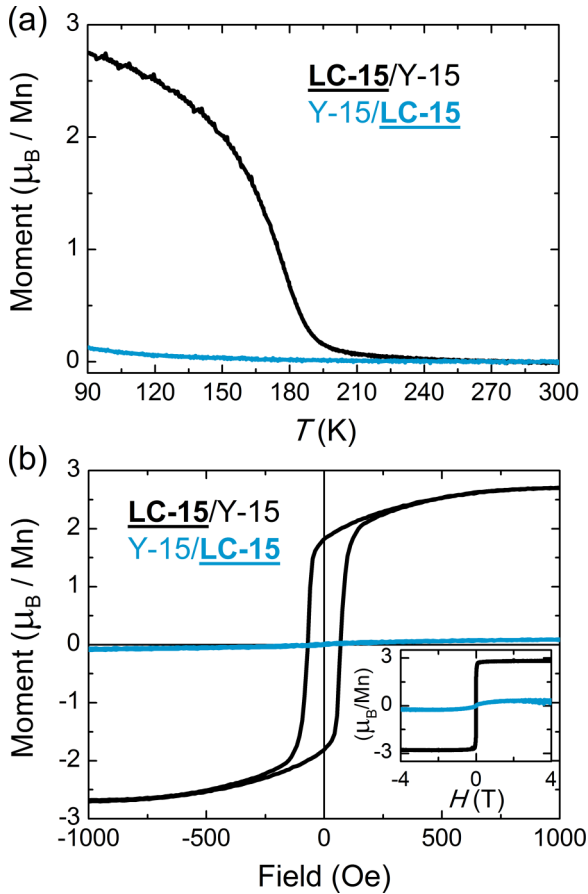FIG. 5. DC magnetization of A-type-grown bilayers LC-15/Y-15 and Y-15/LC-15 that differ only concerning the layer sequence. (a) *M-T* curves obtained while cooling in 1000 Oe parallel to the layers. A clear ferromagnetic transition is observed for LC-15/Y-15 but hardly for Y-15/LC-15, which has a strongly suppressed ferromagnetic moment. (b) *M-H* curves recorded at 100 K (in-plane field). Inset: Same *M-H* curve for an expanded field range up to 4 T.

FIG. 6. DC magnetization of A-type-grown trilayers of Y-10/LC-15/Y-30 and Y-15/LC-15/Y-30 with different thickness of the bottom YBCO layer. (a) *M-T* curves obtained while cooling in 1000 Oe parallel to the layers. A clear ferromagnetic signal with $T^{\text{Curie}} \approx 180\,\text{K}$ is observed for the trilayer with the 10-nm-thick bottom YBCO layer but hardly for the one with the 15-nm-thick bottom YBCO layer. (b) *M-H* curves recorded at 100 K (in-plane field). Inset: Same *M-H* curve with expanded field range up to 4 T.

LC-15/Y-15. This marked suppression of the ferromagnetic moment of the Y-15/LC-15 bilayer is also evident from the magnetization-field (*M-H*) loops at 100 K shown in Fig. 5(b). The LC-15/Y-15 bilayer shows a pronounced ferromagnetic signal with a high field saturation value of about 2.8 μ_{B}/Mn ion and a pronounced hysteresis at low field with a coercive field of $H_{\text{coer}} \approx 70$ Oe and a remnant magnetization of $M_{\text{rem}} \approx 1.8\,\mu_{\text{B}}$/Mn ion. The signal of the bilayer Y-15/LC-15 is again extremely weak, with no clear sign of a hysteresis and a saturation value of only 0.2 μ_{B}/Mn ion. The data in Fig. 5 highlight that the ferromagnetic properties of these 15-nm-thick A-type LCMO layers depend dramatically on whether they are grown directly on the LSAT substrate or on top of an intermediate 15-nm-thick YBCO layer. We have also verified that the magnetic properties of an A-type LSAT/LC-15 single layer without YBCO (data not shown) are very similar to those of the LC-15/Y-15 bilayer and also to those reported in the literature for similarly thin LCMO layers that are directly grown on substrates such as STO, NGO, or even SLAO [30,50].
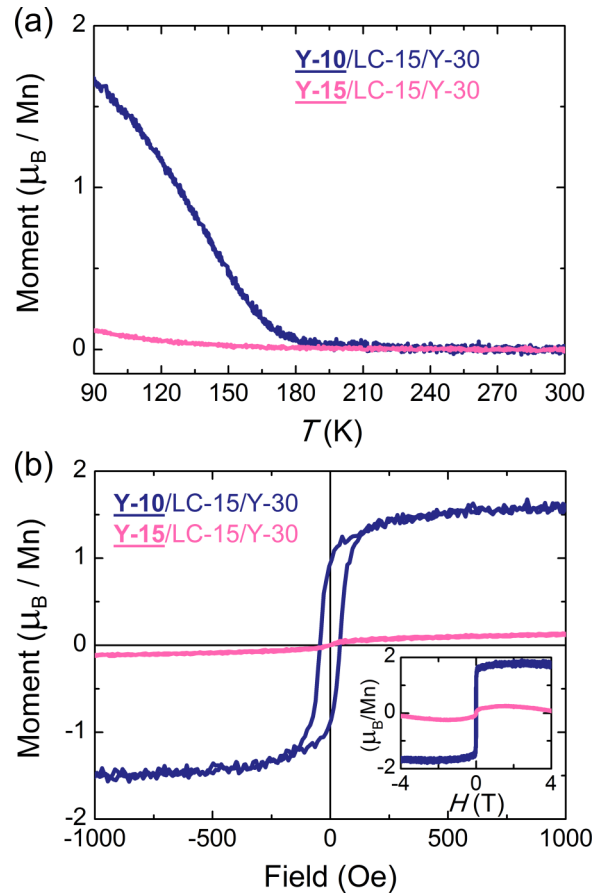
2. DC magnetization of A-type structures with different thickness of intermediate YBCO

The decisive role of the intermediate YBCO layer is further highlighted in Fig. 6, which compares the magnetic response of a Y-15/LC-15/Y-30 trilayer with that of a Y-10/LC-15/Y-30 trilayer. Both samples are almost identical, except for the different thicknesses of the first YBCO layer of $d^{\text{Y}} \approx 15$ and 10 nm, respectively. Figure 6 reveals that this seemingly small difference in the thickness of the intermediate YBCO layer has quite a dramatic effect on the ferromagnetic response of the A-type LCMO layer that is grown on top. For the Y-10/LC-15/Y-30 trilayer (blue symbols) the 1-kOe field-cooled curve in Fig. 6(a) shows a clear ferromagnetic transition with $T^{\text{Curie}} \approx 180\,\text{K}$ and a sizeable magnetic moment of 1.65 μ_{B}/Mn ion at 90 K. Likewise, the *M-H* loop in Fig. 6(b) shows a typical ferromagnetic response with a saturation value of 1.7 μ_{B}/Mn at 5 T and a clear hysteresis around the origin with a coercive field of $H_{\text{coer}} \approx 40$ Oe and a remnant magnetization of $M_{\text{rem}} \approx 0.9\,\mu_{\text{B}}$/Mn ion. To the contrary, the Y-15/LC-15/Y-30 trilayer (pink symbols) shows a very weak

ferromagnetic response, similar to the Y-15/LC-15 bilayer in Fig. 5, with no sign of a hysteresis around the origin and an extremely small saturation moment of $0.12 \mu_B$/Mn ion.

This finding raises the question about the relevant changes of the properties of the YBCO layer that occur upon such a seemingly moderate reduction of the thickness of the YBCO layer from $d^Y = 15$–10 nm. An important factor appears to be the strain relaxation of the YBCO layer that has been reported to occur above a critical thickness of $d^Y_{crit} \approx 15$ nm [30,41]. This strain relaxation typically gives rise to the formation of various structural defects, such as stacking faults or screw dislocations. Moreover, it can affect the orthorhombic distortion of the fully oxygenated YBCO due to the one-dimensional CuO chains along the *b*-axis direction, which most likely remains very small (or short ranged) for the fully strained (unrelaxed) part of the YBCO layer for which the in-plane structure is locked to the one of the cubic LSAT substrate. The length and ordering of the CuO chain segments and the magnitude of the related orthorhombic distortions is likely to increase rapidly as the strain relaxation sets in at $d^Y > d^Y_{crit}$ and the YBCO layer develops its intrinsic structure.

3. DC magnetization of A- and B-type Y-20/LC-30 bilayers

Figure 7 shows that a modification of the growth condition of these multilayers can also give rise to surprisingly large changes of the ferromagnetic properties of the LCMO layers grown on top of YBCO. It displays the magnetization data of two Y-20/LC-30 bilayers that were PLD grown with the conditions A and B as described in Sec. II. Whereas the superconducting transition temperature of $T_c \approx 80$ K of the YBCO layer is very similar (data not shown), their ferromagnetic properties are dramatically different. For the A-type bilayer, the magnetization curve in Fig. 7(a) increases only very gradually toward low temperature and reaches a value of only about $0.3 \mu_B$/Mn ion at 90 K. The corresponding *M-H* loop at 100 K in Fig. 7(b) also shows no sign of a hysteresis around the origin and saturates at $0.3 \mu_B$/Mn ion. To the contrary, the B-type bilayer exhibits a strong ferromagnetic response with a pronounced transition at $T^{Curie} \approx 210$ K and a magnetic moment of $2.8 \mu_B$/Mn at 90 K in Fig. 7(a). The *M-H* loop at 100 K in Fig. 7(b) confirms a large saturation value of $2.8 \mu_B$/Mn and exhibits a pronounced hysteresis around the origin with a coercive field of $H_{coer} \approx 140$ Oe and a remnant magnetization of $M_{rem} \approx 2.15 \mu_B$/Mn ion.

4. Polarized neutron reflectometry of A- and B-type Y-20/LC-30 bilayers

The magnetic depth profile of the same Y-20/LC-30 bilayers for which the dc magnetization is shown in Fig. 7 has been investigated with polarized neutron reflectometry. Figures 8(a) and 8(b) show the reflectivity curves at 300 K (symbols) and the best fit (solid line) from which the depth profile of the nuclear scattering length density, the thickness, and the roughness of the LCMO and YBCO layers have been determined as listed in Table II. Figures 8(c) and 8(d) show the corresponding curves and fits for spin-up and spin-down
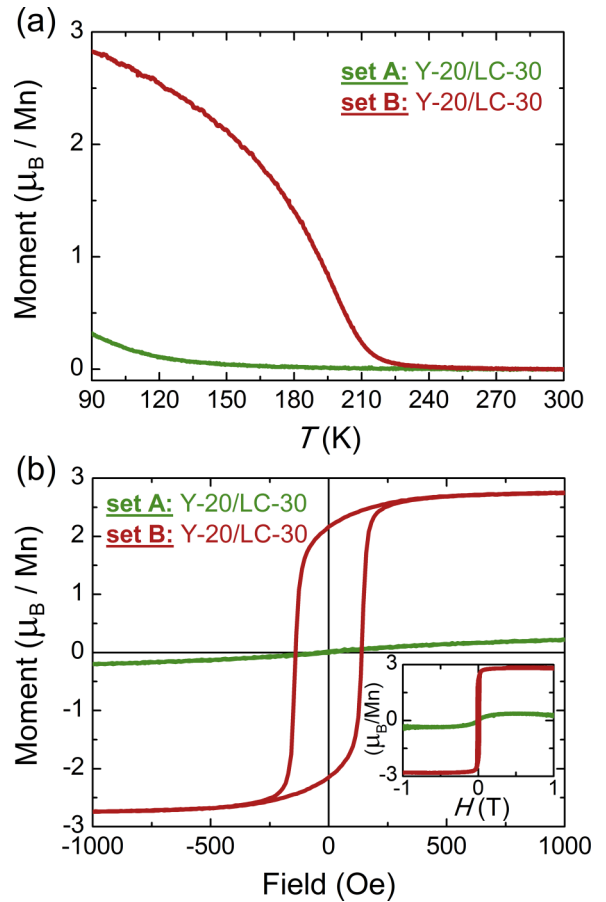

FIG. 7. DC magnetization for two Y-20/LC-30 bilayers grown under A-type (green lines) and B-type (red lines) conditions. (a) *M-T* curves obtained while cooling in 1000 Oe parallel to the layers. The A-type sample shows a strongly suppressed magnetism, while the B-type bilayer exhibits a sharp ferromagnetic transition around $T^{Curie} \approx 210$ K and a large moment of $2.8 \mu_B$/Mn at 90 K. (b) *M-H* curve recorded at 100 K (in-plane field). Inset: Same *M-H* curve with expanded field range up to 1 T.

polarized neutrons in the ferromagnetic state at 90 K. For the B-type bilayer in Fig. 8(d) there is a pronounced splitting between the reflectivity curves for the spin-up and spin-down neutrons that is characteristic of a rather large magnetization of the LCMO layer. For the A-type bilayer in Fig. 8(c) this splitting is very weak and barely visible. To obtain the depth profile of the magnetic scattering length density of these bilayers from the spin-up and spin-down curves at 90 K, the parameters describing the nuclear part were fixed to those obtained from the 300-K curves. Figures 8(e) and 8(f) show the magnetic depth profiles (blue lines) that have been obtained from the best fits that are displayed by the solid lines in Figs. 8(c) and 8(d). For the A-type bilayer they confirm a strong suppression of the ferromagnetic moment of the LCMO layer and yield a dead layer with a thickness on the order of about 20 nm and an average moment of $0.30 \mu_B$/Mn ion. To the contrary, for the B-type bilayer they yield a large ferromagnetic moment with an average value of $3.27 \mu_B$/Mn that agrees well with that deduced from dc magnetization
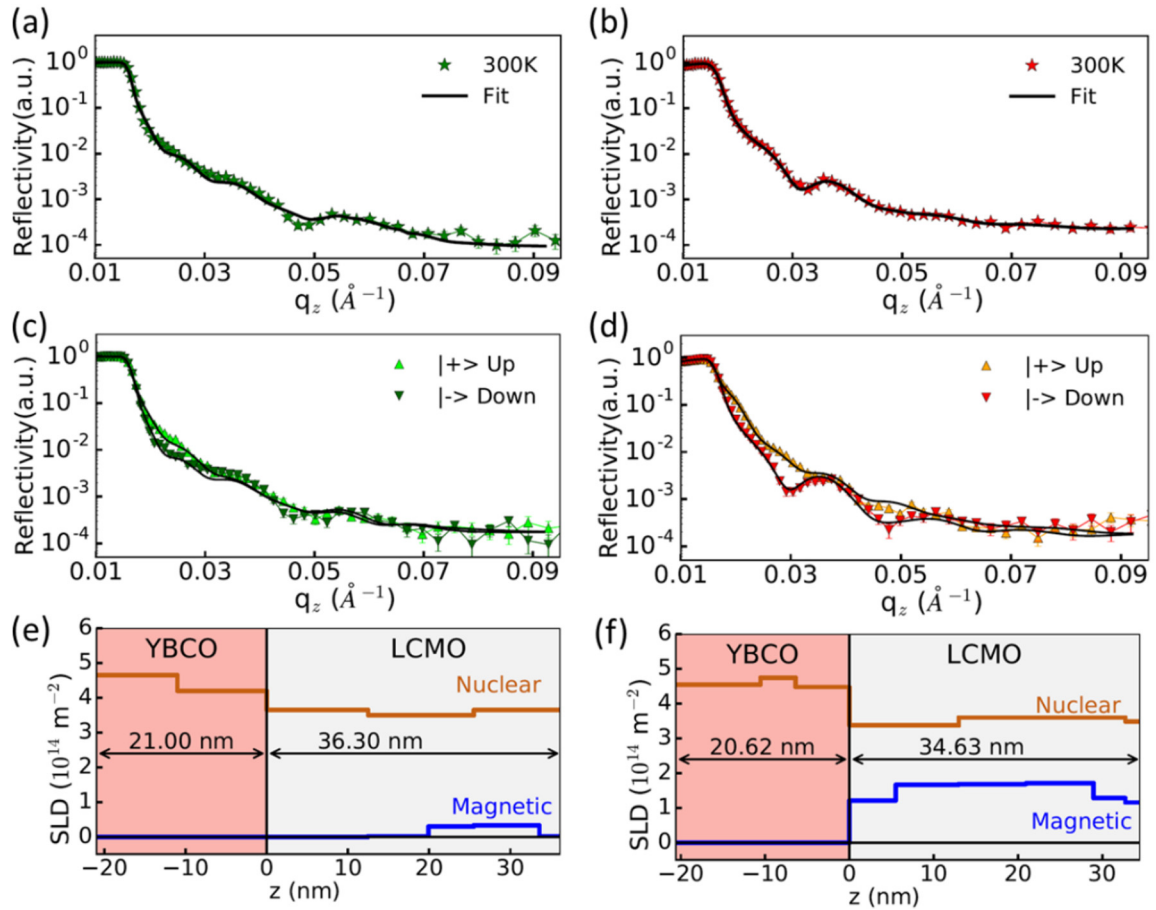
FIG. 8. Polarized neutron reflectometry (PNR) curves of A- and B-type Y-20/LC-30 bilayers. (a, b) Reflectivity curves (symbols) and fits (lines) of the A- and B-type bilayers, respectively, obtained in the paramagnetic state at 300 K for which the spin-up and spin-down signals are identical. (c, d) Corresponding polarized reflectivity curves (symbols) and fits (lines) obtained at 90 K in the ferromagnetic state of LCMO. (e, f) Depth profiles of the nuclear (brown line) and magnetic (blue line) scattering length densities obtained from fitting the reflectivity curves of the A- and B-type bilayers, respectively.

(see Fig. 7). Furthermore, this B-type bilayer has only a thin "dead layer" at the YBCO/LCMO interface of about 5.5 nm for which the magnetization is reduced but not even fully suppressed.

5. Enhanced DC magnetization for multilayers with cation-substituted, tetragonal YBCO

To test the hypothesis that the orthorhombic distortions due to the long-range order of the CuO chains of YBCO contribute

TABLE II. Parameters used to fit the polarized neutron reflectometry data of the A-type and B-type Y-20/LC-30 bilayers.

| Layer	A type			B type		
	Thickness (nm)	SLD (10^{14} m^{-2})	$M(\mu_B/\text{Mn})$	Thickness (nm)	SLD (10^{14} m^{-2})	$M(\mu_B/\text{Mn})$
LCMO$_6$	2.70 ± 0.25	3.65	0.10	1.90 ± 0.30	3.48	2.47
LCMO$_5$	8.00 ± 0.20	3.65	0.80	3.70 ± 0.40	3.60	2.74
LCMO$_4$	5.60 ± 0.26	3.50	0.64	8.00 ± 0.33	3.60	3.65
LCMO$_3$	7.50 ± 0.13	3.50	0.10	8.00 ± 0.32	3.60	3.60
LCMO$_2$	5.50 ± 0.30	3.65	0.00	7.50 ± 0.10	3.37	3.55
LCMO$_1$	7.00 ± 0.06	3.65	0.00	5.50 ± 0.20	3.37	2.50
YBCO$_3$	11.00 ± 0.20	4.20		6.30 ± 0.25	4.47	
YBCO$_2$	5.00 ± 0.10	4.65		4.10 ± 0.10	4.74	
YBCO$_1$	5.00 ± 0.10	4.65		10.00 ± 0.24	4.54	
			LSAT substrate			
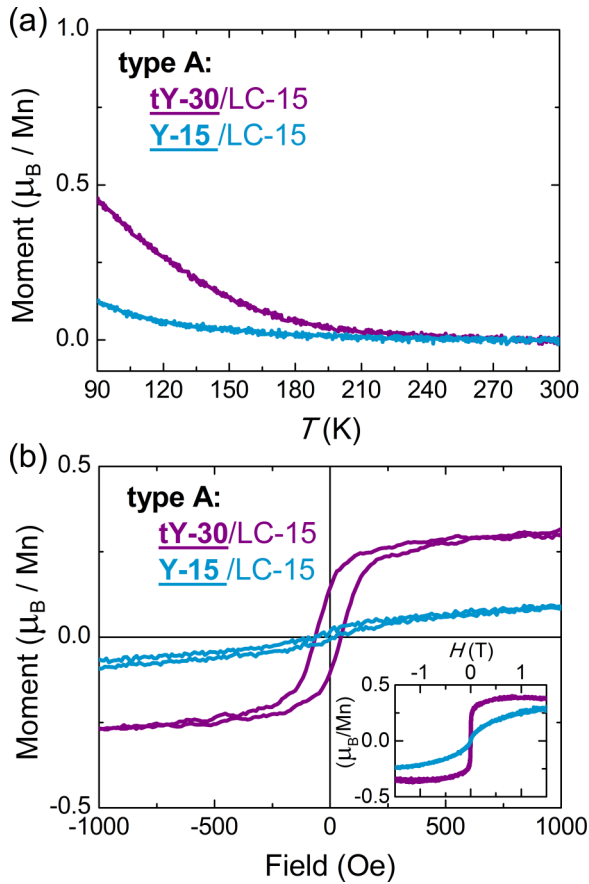
FIG. 9. DC magnetization data of the A-type bilayers tY-30/LC-15 and Y-15/LC-15. (a) *M-T* curves obtained while cooling in 1000 Oe parallel to the layers. tY-30/LC-15 exhibits a larger ferromagnetic response than Y-15/LC-15, despite of having a cuprate intermediate layer two times thicker with $T^{Curie} \approx 180$ K. (b) *M-H* curves recorded at 100 K (in-plane field). Inset: Same *M-H* curves with expanded field range up to 1.5 T.

FIG. 10. DC magnetization data of the B-type trilayers Y-100/LC-10/Y-100 and tY-100/LC-10/Y-100. (a) *M-T* curves obtained while cooling in 1000 Oe parallel to the layers. A transition to a ferromagnetic state is observed in both cases at $T^{Curie} \approx 200$ K, but a considerably larger magnetization at 90 K is obtained for the tY-100/LC-10/Y-100 trilayer. (b) *M-H* curves recorded at 100 K (in-plane field). Inset: Same *M-H* curves with expanded field range up to 1 T.

to the strong suppression of the ferromagnetic order of LCMO layers that are grown on top, we studied corresponding multilayers with intermediate $Y_{0.8}Ca_{0.2}Ba_2Cu_{2.8}Co_{0.2}O_7$ layers. The Co^{3+} ions are incorporated mainly within the CuO chains and give rise to a strong structural disorder that suppresses the orthorhombicity of YBCO. For bulk YBCO crystals, a quasitetragonal structure without any long-range order of the CuO chains is thus obtained for a Co content $y > 0.15$ [51]. The additional partial substitution of Ca^{2+} on the Y^{3+} site is used to counteract the electron doping due to the Co^{3+} substitution, and thus to maintain an almost optimal doping level with a reasonably high superconducting transition temperature of $T_c \approx 73$ K for these tetragonal $Y_{0.8}Ca_{0.2}Ba_2Cu_{2.8}Co_{0.2}O_7$ (tYBCO) layers.

Figure 9 compares the magnetization data of the A-type Y-15/LC-15 bilayer, which are also shown in Fig. 5 and discussed in Sec. III C 1, with those of an A-type-grown tY-30/LC-15 bilayer. It is evident that the latter tY-30/LC-15 bilayer exhibits a much stronger ferromagnetic signal than the former Y-15/LC-15 bilayer, for which the ferromagnetic signal is extremely weak. The ferromagnetic signal arising in tY-30/LC-15 in Fig. 9(a) demonstrates a magnetic
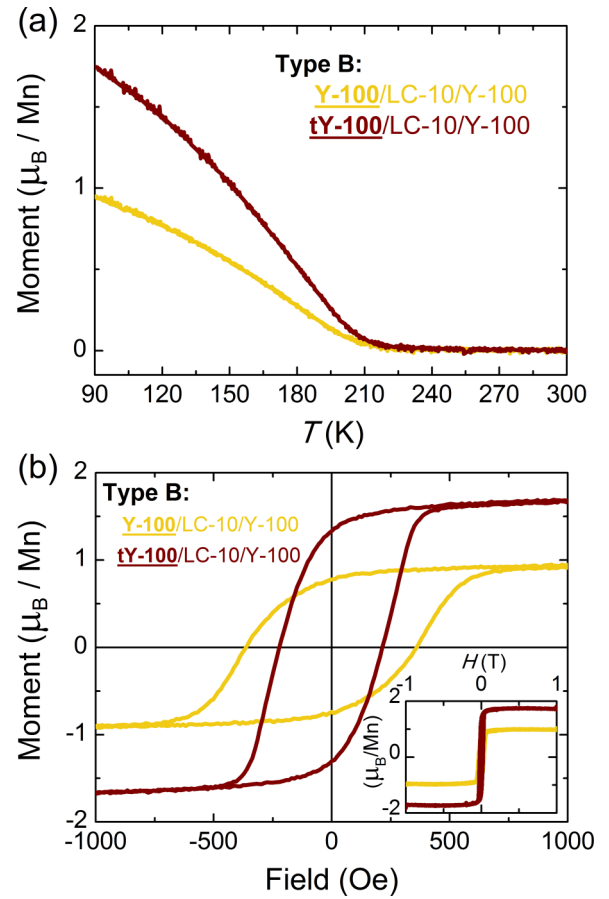
activation at temperature of about $T^{Curie} \approx 180$ K that reaches 0.45 μ_B/Mn at 90 K. Furthermore, hysteresis is found around zero field in the in-plane *M-H* curves obtained at 100 K, shown in Fig. 9(b), with a finite coercive field of $H_{coer} \approx 55$ Oe and a remnant magnetization of $M_{rem} \approx 0.14$ μ_B/Mn ion. The moment rapidly saturates with field [see inset in Fig. 9(b)], reaching 0.38 μ_B/Mn ion at 1.5 T. Note that this enhancement occurs despite the much larger (doubled) thickness of the intermediate tetragonal YBCO layer, which for the case of orthorhombic YBCO has been shown to be detrimental to the magnetic properties of a LCMO layer that is grown on top (see Fig. 6 and the discussion in Sec. III C 2). This comparison thus demonstrates that the suppression of the ferromagnetic signal of the LCMO layer is less pronounced if it is grown on top of a tetragonal YBCO (tY) layer rather than on the regular orthorhombic YBCO.

Figure 10 shows that the tetragonal YBCO can also be used in B-type multilayers to enhance the ferromagnetism of thin LCMO layers that are grown on top of very thick YBCO layers. It compares the magnetization curves of a

Y-100/LC-10/Y-100 trilayer (yellow symbols) and a corresponding tY-100/LC-10/Y-100 trilayer (red symbols) that are both B-type grown. Figure 10(a) shows that whereas both trilayers have similar Curie temperatures of $T^{Curie} \approx 200$ K, the magnetization of tY-100/LC-10/Y-100 is considerably larger with 1.75 μ_B/Mn at 90 K than for Y-100/LC-10/Y-100 with 0.9 μ_B/Mn at 90 K. A corresponding difference is also evident for the *M-H* curves in Fig. 10(b), for which both trilayers exhibit a pronounced hysteresis around the origin with coercive fields of $H_{coer} \approx 360$ and 220 Oe and remnant magnetizations of $M_{rem} \approx 0.7$ and 1.3 μ_B/Mn ion for trilayers with the intermittent Y-100 and tY-100 layers, respectively. The rather strong enhancement of the coercive field of Y-100/LC-10/Y-100 is typical for multilayers for which a thin LCMO layer is grown on top of a very thick YBCO layer and is likely also related to the orthorhombic distortion of the latter. The inset of Fig. 10(b) shows that the high field saturation value amounts to 0.95 μ_B/Mn for Y-100/LC-10/Y-100 as compared to 1.75 μ_B/Mn for tY-100/LC-10/Y-100.

6. Superconducting spin-valve structures with very thin manganite layers and large, switchable magnetization

Last but not least, we show in Fig. 11 the corresponding dc magnetization data of a more complex multilayer structure with very thick superconducting layers and two very thin LCMO and LSMO ferromagnetic layers. The profile of the multilayer, following the formalism used, is tY-100/LS-5/Y-4/LC-10/Y-100. This sample was made in an attempt to grow a superconducting spin-valve structure for which two thick superconducting (YBCO and tYBCO) electrode layers are separated by two very thin ferromagnetic layers that have a strong magnetic response with different coercive fields, such that their magnetization direction can be individually switched with an external magnetic field. Figure 11 confirms that we managed to obtain a strong ferromagnetic order within the LCMO and LSMO layers, even though they are very thin and grown on top of a 100-nm-thick tYBCO layer. Figure 11(a) shows the *M-T* curve for this multilayer, with a magnetic moment building above 300 K that arises from the LSMO layers with $T^{Curie} > 300$ K, and a strong, additional enhancement at lower temperature that can be assigned to the LCMO layer with $T^{Curie} \approx 210$ K. The *M-H* loop in Fig. 11(b) confirms that the LCMO and LSMO layers have different coercive fields of about 300 and 40 Oe, respectively, and that their magnetization can indeed be independently switched, as is seen by the two-step behavior of the hysteresis loop, which is most clearly seen in the derivative plot of *dM/dH*. This demonstrates that even very thin LCMO and LSMO layers with a rather strong ferromagnetic response can be embedded between thick YBCO layers if the growth parameters are optimized to ensure a stoichiometric composition. We believe that it is a first promising step toward the growth of SC/FM multilayers from these complex oxides that can be used to study the spin-valve effect and related quantum spintronic phenomena.

IV. DISCUSSION AND SUMMARY

The results described above reveal that the ferromagnetic properties of a LCMO layer that is grown with pulsed laser de-
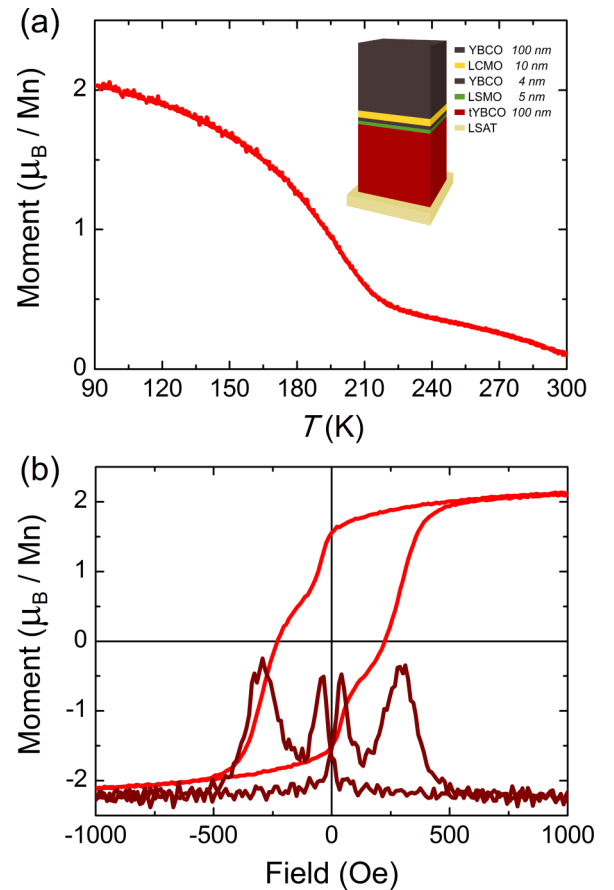

FIG. 11. DC magnetization data of a spin-valve-type multilayer with two very thin manganite layers. (a) *M-T* curve obtained while cooling in 1000 Oe parallel to the layers. A clear ferromagnetic transition due to the LCMO layer is observed at $T^{Curie} \approx 210$ K. The corresponding ferromagnetic transition of the LSMO layer occurs above 300 K. (b) *M-H* curves recorded at 90 K (in-plane field). The hysteresis loop has a two-step transition that is most clearly seen in the corresponding derivative curve (darker line). The peaks of the latter mark the coercive fields of $H_{coer} \approx 40$ and 300 Oe for LSMO and LCMO, respectively.

position (PLD) on top of the cuprate high-T_c superconductor YBa$_2$Cu$_3$O$_7$ (YBCO) are very sensitive to growth conditions and strongly dependent on the structural details of the YBCO layer. We have shown that thin LCMO layers that are prepared with the A-type conditions (described in Table I) exhibit a strong ferromagnetic response if grown directly on a LSAT substrate, whereas their ferromagnetic moment is drastically reduced when they are grown on an intermediate YBCO layer. Moreover, Fig. 6 reveals that the thickness of the intermediate YBCO layer plays an important role in the suppression of the ferromagnetic moment of the A-type LCMO layers. This suggests that the dislocations and defects related to the strain relaxation that sets in above a critical YBCO layer thickness of about 15 nm [30,41] are detrimental to the ferromagnetic order of the LCMO layer on top. Likewise, we have obtained evidence for a negative impact due to the orthorhombic structure of YBCO that arises when the one-dimensional CuO chains develop a long-range order. This hypothesis has

been confirmed by replacing the orthorhombic YBCO with tetragonal $Y_{0.8}Ca_{0.2}Ba_2Cu_{2.8}Co_{0.2}O_7$ (tY), for which the CuO chains are strongly disrupted by the Co ions which prefer a threefold oxygen coordination. The data in Fig. 9 confirm that the ferromagnetic moment of an A-type tY-30/LC-15 bilayer is more than doubled as compared to an A-type Y-15/LC-15 bilayer with only half the YBCO layer thickness.

Moreover, we have shown that by using the modified B-type growth conditions (detailed in Table I) one can obtain LCMO layers with a strong ferromagnetic order that is far less sensitive to the structural details of the intermediate YBCO layer. The dramatic differences between the ferromagnetic properties of such A- and B-type multilayers have been demonstrated for a pair of Y-20/LC-30 bilayers for which the average magnetization and magnetic depth profile have been measured with dc magnetization and polarized neutron reflectometry. For the B-type bilayer they revealed a bulklike ferromagnetic order with an average magnetic moment of $3.27 \mu_B$/Mn ion at 90 K without a dead layer at the LCMO/YBCO interface. In stark contrast, for the A-type bilayer they revealed only a very weak ferromagnetic response with an average moment of $0.30 \mu_B$/Mn ions and a thick dead layer of about 20 nm next to the YBCO/LCMO interface for which the ferromagnetic order is entirely absent.

Finally, we have demonstrated that using a B-type growth mode and tetragonal $Y_{0.8}Ca_{0.2}Ba_2Cu_{2.8}Co_{0.2}O_7$ (tYBCO) layers allows one to obtain very thin LCMO layers (10 nm) with a strong ferromagnetic response on top of very thick tYBCO layers (100 nm). Last but not least, the data in Fig. 11 highlight that this approach enables the growth of spin-valve structures with thick YBCO electrodes and, yet, two very thin manganite layers with sizeable ferromagnetic moments whose relative orientation can be readily adjusted with an external magnetic field.

These observations raise the important question as to why the ferromagnetic properties of the A-type LCMO layers are so strongly affected by the structural details of the intermediate YBCO layer on which they are grown, whereas the ferromagnetism of the B-type samples is much more robust. The structural analysis based on the XRD and scanning transmission electron microscopy (STEM) data suggests that both the A- and B-type multilayers have a high structural quality with epitaxial YBCO and LCMO layers that have flat and sharp interfaces and show no signs of chemical interdiffusion. The most pronounced difference between these A- and B-type samples is identified from the analysis of the STEM-EELS data and concerns the average oxidation state of the Mn ions. Whereas for the B-type samples it is close to the nominal value of $+3.3$, for the A-type samples it is strongly enhanced up to about $+3.5$. Such a pronounced increase of the Mn oxidation state and thus of the hole doping of the A-type LCMO layers arises most likely from a nonideal cation stoichiometry due to a deficiency of the La and/or Mn ions. A corresponding cation deficiency has also been observed in nominally undoped $LaMnO_3$ thin-film samples for which the additional hole doping gives rise to a ferromagnetic order instead of the antiferromagnetic state of the undoped parent compound [43].

For the present A-type LCMO layers the cation deficiency weakens the ferromagnetic order in two ways. First, it enhances the hole doping and thus places them in the doping phase diagram close to a phase boundary between the itinerant ferromagnetic order at $x < 0.5$ and the antiferromagnetic and charge/orbital ordered states at $x > 0.5$ [15,16]. The ferromagnetic properties near this phase boundary are known to be very sensitive to defects and lattice distortions which reduce the bandwidth and thus the strength of the double-exchange interaction. Secondly, the Mn vacancies are directly disrupting the network of Mn-O-Mn bonds and thereby further reduce the effective bandwidth and the ferromagnetic double-exchange interaction, thus favoring antiferromagnetic and/or glassy types of magnetic orders [15,16,43].

In summary, we have shown that the ferromagnetic order of LCMO layers that are grown with pulsed laser deposition on an intermediate YBCO layer can be strongly dependent on the PLD growth conditions. A moderate variation of the growth parameters can result in a significant cation deficiency, which increases the hole doping of the LCMO layer and thus places it close to a phase boundary in the doping phase diagram at which the ferromagnetic order is easily suppressed in favor of an antiferromagnetic and/or glassy state. Even minor strain effects and defects that arise from the relaxation and the orthorhombic distortion of the underlying YBCO layer can therefore give rise to a strong suppression of the ferromagnetic order and induce a very thick dead layer. Furthermore, we have demonstrated that with PLD one can grow samples with stoichiometric LCMO layers with the nominal hole doping close to $x = 0.33$, for which the ferromagnetic order is very robust and hardly dependent on the structural details of the underlying YBCO layer. Very thin (10 nm) and strongly ferromagnetic LCMO layers thus can be readily grown on top of thick YBCO layers (100 nm). Even superconducting spin-valve structures with two such thin ferromagnetic manganite layers can be prepared for which the magnetization direction can be switched independently with an external magnetic field. Such superconductor/ferromagnet heterostructures with very thick bottom electrodes and, yet, very thin ferromagnetic layers with sizeable and individually switchable magnetic moments are of great interest in fundamental and applied science. For certain noncollinear magnetic arrangements they allow one to induce a superconducting order parameter with a large spin-triplet component that can be a source of spin-polarized supercurrents for superspintronic devices or memory cells [1–6].

[1] L. N. Bulaevskii, A. I. Buzdin, M. L. Kuli, and S. V. Panjukov, Coexistence of superconductivity and magnetism theoretical predictions and experimental results, Adv. Phys. **34**, 175 (1985).

[2] A. Buzdin, Mixing superconductivity and magnetism, Nat. Mater. **3**, 751 (2004).

[3] J. Linder and J. W. A. Robinson, Superconducting spintronics, Nat. Phys. **11**, 307 (2015).

[4] J. W. A. Robinson, J. D. S. Witt, and M. G. Blamire, Controlled injection of spin-triplet supercurrents into a strong ferromagnet, Science **329**, 59 (2010).

[5] T. S. Khaire, M. A. Khasawneh, W. P. Pratt, and N. O. Birge, Observation of Spin-Triplet Superconductivity in Co-Based Josephson Junctions, Phys. Rev. Lett. **104**, 137002 (2010).

[6] M. Eschrig, Spin-polarized supercurrents for spintronics, Phys. Today **64**(1), 43 (2011).

[7] K. Dybko, K. Werner-Malento, P. Aleshkevych, M. Wojcik, M. Sawicki, and P. Przyslupski, Possible spin-triplet superconducting phase in the $La_{0.7}Sr_{0.3}MnO_3/YBa_2Cu_3O_7/La_{0.7}Sr_{0.3}MnO_3$ trilayer, Phys. Rev. B **80**, 144504 (2009).

[8] Y. Kalcheim, T. Kirzhner, G. Koren, and O. Millo, Long-range proximity effect in $La_{2/3}Ca_{1/3}MnO_3/(100)YBa_2Cu_3O_{7-\delta}$ ferromagnet/superconductor bilayers: Evidence for induced triplet superconductivity in the ferromagnet, Phys. Rev. B **83**, 064510 (2011).

[9] C. Visani, Z. Sefrioui, J. Tornos, C. Leon, J. Briatico, M. Bibes, A. Barthélémy, J. Santamaría, and J. E. Villegas, Equal-spin Andreev reflection and long-range coherent transport in high-temperature superconductor/half-metallic ferromagnet junctions, Nat. Phys. **8**, 539 (2012).

[10] T. Golod, A. Rydh, V. M. Krasnov, I. Marozau, M. A. Uribe-Laverde, D. K. Satapathy, T. Wagner, and C. Bernhard, High bias anomaly in $YBa_2Cu_3O_{7-x}/LaMnO_{3+\delta}/YBa_2Cu_3O_{7-x}$ superconductor/ferromagnetic insulator/superconductor junctions: Evidence for a long-range superconducting proximity effect through the conduction band of a ferromagnetic insulator, Phys. Rev. B **87**, 134520 (2013).

[11] M. Egilmez, J. W. A. Robinson, J. L. MacManus-Driscoll, L. Chen, H. Wang, and M. G. Blamire, Supercurrents in half-metallic ferromagnetic $La_{2/3}Ca_{1/3}MnO_3$, EPL **106**, 37003 (2014).

[12] E. Dagotto, When oxides meet face to face, Science **318**, 1076 (2007).

[13] M. Imada, A. Fujimori, and Y. Tokura, Metal-insulator transitions, Rev. Mod. Phys. **70**, 1039 (1998).

[14] H. Y. Hwang, Y. Iwasa, M. Kawasaki, B. Keimer, N. Nagaosa, and Y. Tokura, Emergent phenomena at oxide interfaces, Nat. Mater. **11**, 103 (2012).

[15] Y. Tokura and Y. Tomioka, Colossal magnetoresistive manganites, J. Magn. Magn. Mater. **200**, 1 (1999).

[16] Y. Tokura, Critical features of colossal magnetoresistive manganites, Rep. Prog. Phys. **69**, 797 (2006).

[17] P. Przyslupsk, S. Kolesnik, E. Dynowska, T. Skoskiewicz, and M. Sawicki, Fabrication and properties of $YBa_2Cu_3O_{7-x}/RE_{1-x}A_xMnO_{3-y}$ multilayers, IEEE Trans. Appl. Supercond. **7**, 2192 (1997).

[18] M. Goldman, P. I. Kraus, K. Nikolaev, V. Vas'ko, A. Bhattacharya, and W. Cooley, Spin injection and transport in magnetic-superconducting oxide heterostructures, J. Supercond. **14**, 283 (2001).

[19] H.-U. Habermeier and G. Cristiani, Cuprate/ferromagnetic oxide superlattices, J. Supercond. **15**, 425 (2002).

[20] Z. Sefrioui, D. Arias, V. Peña, J. E. Villegas, M. Varela, P. Prieto, C. León, J. L. Martínez, and J. Santamaría, Ferromagnetic/superconducting proximity effect in $La_{0.7}Ca_{0.3}MnO_3/YBa_2Cu_3O_{7-\delta}$ superlattices, Phys. Rev. B **67**, 214511 (2003).

[21] T. Holden, H.-U. Habermeier, G. Cristiani, A. Golnik, A. Boris, A. Pimenov, J. Humlíček, O. I. Lebedev, G. Van Tendeloo, B. Keimer, and C. Bernhard, Proximity induced metal-insulator transition in $YBa_2Cu_3O_7/La_{2/3}Ca_{1/3}MnO_3$ superlattices, Phys. Rev. B **69**, 064505 (2004).

[22] V. Peña, Z. Sefrioui, D. Arias, C. León, J. Santamaría, J. L. Martinez, S. G. E. te Velthuis, and A. Hoffmann, Giant Magnetoresistance in Ferromagnet/Superconductor Superlattices, Phys. Rev. Lett. **94**, 057002 (2005).

[23] J. Stahn, J. Chakhalian, C. Niedermayer, J. Hoppler, T. Gutberlet, J. Voigt, F. Treubel, H.-U. Habermeier, G. Cristiani, B. Keimer, and C. Bernhard, Magnetic proximity effect in perovskite superconductor/ferromagnet multilayers, Phys. Rev. B **71**, 140509(R) (2005).

[24] A. Hoffmann, S. G. E. te Velthuis, Z. Sefrioui, J. Santamaría, M. R. Fitzsimmons, S. Park, and M. Varela, Suppressed magnetization in $La_{0.7}Ca_{0.3}MnO_3/YBa_2Cu_3O_{7-\delta}$ superlattices, Phys. Rev. B **72**, 140407(R) (2005).

[25] W. Luo, S. J. Pennycook, and S. T. Pantelides, Magnetic "Dead" Layer at a Complex Oxide Interface, Phys. Rev. Lett. **101**, 247204 (2008).

[26] D. K. Satapathy, M. A. Uribe-Laverde, I. Marozau, V. K. Malik, S. Das, T. Wagner, C. Marcelot, J. Stahn, S. Brück, A. Rühm, S. Macke, T. Tietze, E. Goering, A. Frañó, J. H. Kim, M. Wu, E. Benckiser, B. Keimer, A. Devishvili, B. P. Toperverg *et al.*, Magnetic Proximity Effect in $YBa_2Cu_3O_7/La_{2/3}Ca_{1/3}MnO_3$ and $YBa_2Cu_3O_7/LaMnO_{3+\delta}$ Superlattices, Phys. Rev. Lett. **108**, 197201 (2012).

[27] M. A. Uribe-Laverde, D. K. Satapathy, I. Marozau, V. K. Malik, S. Das, K. Sen, J. Stahn, A. Rühm, J.-H. Kim, T. Keller, A. Devishvili, B. P. Toperverg, and C. Bernhard, Depth profile of the ferromagnetic order in a $YBa_2Cu_3O_7/La_{2/3}Ca_{1/3}MnO_3$ superlattice on a LSAT substrate: A polarized neutron reflectometry study, Phys. Rev. B **87**, 115105 (2013).

[28] K. Sen, E. Perret, A. Alberca, M. A. Uribe-Laverde, I. Marozau, M. Yazdi-Rizi, B. P. P. Mallett, P. Marsik, C. Piamonteze, Y. Khaydukov, M. Döbeli, T. Keller, N. Biškup, M. Varela, J. Vašátko, D. Munzar, and C. Bernhard, X-ray absorption study of the ferromagnetic Cu moment at the $YBa_2Cu_3O_7/La_{2/3}Ca_{1/3}MnO_3$ interface and variation of its exchange interaction with the Mn moment, Phys. Rev. B **93**, 205131 (2016).

[29] A. Alberca, M. A. Uribe-Laverde, Y. W. Windsor, M. Ramakrishnan, L. Rettig, I. Marozau, J.-M. Tonnerre, J. Stahn, U. Staub, and C. Bernhard, Element-specific magnetization redistribution at $YBa_2Cu_3O_7/La_{2/3}Ca_{1/3}MnO_3$ interfaces, Phys. Rev. B **92**, 174415 (2015).

[30] V. K. Malik, I. Marozau, S. Das, B. Doggett, D. K. Satapathy, M. A. Uribe-Laverde, N. Biškup, M. Varela, C. W. Schneider, C. Marcelot, J. Stahn, and C. Bernhard, Pulsed laser deposition growth of heteroepitaxial $YBa_2Cu_3O_7/La_{0.67}Ca_{0.33}MnO_3$ superlattices on $NdGaO_3$ and $Sr_{0.7}La_{0.3}Al_{0.65}Ta_{0.35}O_3$ substrates, Phys. Rev. B **85**, 054514 (2012).

[31] C. L. Prajapat, S. Singh, A. Paul, D. Bhattacharya, M. R. Singh, S. Mattauch, G. Ravikumar, and S. Basu, Superconductivity-induced magnetization depletion in a ferromagnet through an insulator in a ferromagnet-insulator-superconductor hybrid oxide heterostructure, Nanoscale **8**, 10188 (2016).

[32] C. L. Prajapat, S. Singh, D. Bhattacharya, G. Ravikumar, S. Basu, S. Mattauch, J.-G. Zheng, T. Aoki, and A. Paul, Proximity effects across oxide-interfaces of superconductor-insulator-ferromagnet hybrid heterostructure, Sci. Rep. **8**, 3732 (2018).

[33] O. H. C. Paull, A. V. Pan, G. L. Causer, S. A. Fedoseev, A. Jones, X. Liu, A. Rosenfeld, and F. Klose, Field dependence of the ferromagnetic/superconducting proximity effect in a YBCO/STO/LCMO multilayer, Nanoscale **10**, 18995 (2018).

[34] S. R. Giblin, J. W. Taylor, J. A. Duffy, M. W. Butchers, C. Utfeld, S. B. Dugdale, T. Nakamura, C. Visani, and J. Santamaría, Measurement of Magnetic Exchange in Ferromagnet-Superconductor $La_{2/3}Ca_{1/3}MnO_3/YBa_2Cu_3O_7$ Bilayers, Phys. Rev. Lett. **109**, 137005 (2012).

[35] A. Tebano, A. Orsini, P. G. Medaglia, D. Di Castro, G. Balestrino, B. Freelon, A. Bostwick, Young Jun Chang, G. Gaines, E. Rotenberg, and N. L. Saini, Preferential occupation of interface bands in $La_{2/3}Sr_{1/3}MnO_3$ films as seen via angle-resolved photoemission, Phys. Rev. B **82**, 214407 (2010).

[36] J. Chakhalian, J. W. Freeland, G. Srajer, J. Strempfer, G. Khaliullin, J. C. Cezar, T. Charlton, R. Dalgliesh, C. Bernhard, G. Cristiani, H.-U. Habermeier, and B. Keimer, Magnetism at the interface between ferromagnetic and superconducting oxides, Nat. Phys. **2**, 244 (2006).

[37] J. Stahn and A. Glavic, Focusing neutron reflectometry: Implementation and experience on the TOF-reflectometer AMOR, Nucl. Instrum. Methods Phys. Res. A **821**, 44 (2016).

[38] J. Stahn and A. Glavic, Efficient polarization analysis for focusing neutron instruments, J. Phys. Conf. Ser. **862**, 012007 (2017).

[39] J. Gazquez, R. Guzman, R. Mishra, E. Bartolomé, J. Salafranca, C. Magén, M. Varela, M. Coll, A. Palau, S. M. Valvidares, P. Gargiani, E. Pellegrin, J. Herrero-Martin, S. J. Pennycook, S. T. Pantelides, T. Puig, and X. Obradors, Emerging diluted ferromagnetism in high-Tc superconductors driven by point defect clusters, Adv. Sci. **3**, 1500295 (2016).

[40] M. Varela, M. P. Oxley, W. Luo, J. Tao, M. Watanabe, A. R. Lupini, S. T. Pantelides, and S. J. Pennycook, Atomic-resolution imaging of oxidation states in manganites, Phys. Rev. B **79**, 085117 (2009).

[41] B. Dam, J. M. Huijbregtse, and J. H. Rector, Strong pinning linear defects formed at the coherent growth transition of pulsed-laser-deposited $YBa_2Cu_3O_{7-\delta}$ films, Phys. Rev. B **65**, 064528 (2002).

[42] G. A. Botton, C. C. Appel, A. Horsewell, and W. M. Stobbs, Quantification of the EELS near-edge structures to study Mn doping in oxides, J. Microsc. **180**, 211 (1995).

[43] I. Marozau, P. T. Das, M. Döbeli, J. G. Storey, M. A. Uribe-Laverde, S. Das, C. Wang, M. Rössle, and C. Bernhard, Influence of La and Mn vacancies on the electronic and magnetic properties of $LaMnO_{3+\delta}$ thin films grown by pulsed laser deposition, Phys. Rev. B **89**, 174422 (2014).

[44] J. Töpfer and J. B. Goodenough, $LaMnO_{3+\delta}$ revisited, J. Solid State Chem. **130**, 117 (1997).

[45] J. H. Kuo, H. U. Anderson, and D. M. Sparlin, Oxidation-reduction behavior of undoped and Sr-doped $LaMnO_3$ nonstoichiometry and defect structure, J. Solid State Chem. **83**, 52 (1989).

[46] C. Ritter, M. R. Ibarra, J. M. De Teresa, P. A. Algarabel, C. Marquina, J. Blasco, J. García, S. Oseroff, and S.-W. Cheong, Influence of oxygen content on the structural, magnetotransport, and magnetic properties of $LaMnO_{3+\delta}$, Phys. Rev. B **56**, 8902 (1997).

[47] J. A. M. V. Roosmalen, E. H. P. Cordfunke, R. B. Helmholdt, and H. W. Zandbergen, The defect chemistry of $LaMnO_{3+\delta}$: 2. Structural aspects of $LaMnO_{3+\delta}$, J. Solid State Chem. **110**, 100 (1994).

[48] M. Varela, A. R. Lupini, S. J. Pennycook, Z. Sefrioui, and J. Santamaría, Nanoscale analysis of $YBa_2Cu_3O_{7-x}$/ $La_{0.67}Ca_{0.33}MnO_3$ interfaces, Solid-State Electron. **47**, 2245 (2003), Proceedings of the 9th International Workshop on Oxide Electronics.

[49] J. Salafranca, J. Rincoón, J. Tornos, C. Leoón, J. Santamaría, E. Dagotto, S. J. Pennycook, and M. Varela, Competition between Covalent Bonding and Charge Transfer at Complex-Oxide Interfaces, Phys. Rev. Lett. **112**, 196802 (2014).

[50] J. Dvorak, Y. U. Idzerda, S. B. Ogale, S. Shinde, T. Wu, T. Venkatesan, R. Godfrey, and R. Ramesh, Are strain-induced effects truly strain induced? A comprehensive study of strained LCMO thin films, J. Appl. Phys. **97**, 10C102 (2005).

[51] F. Maury, I. Mirebeau, J. A. Hodges, P. Bourges, Y. Sidis, and A. Forget, Long- and short-range magnetic order, charge transfer, and superconductivity in $YBa_2Cu_{3-x}Co_xO_7$, Phys. Rev. B **69**, 094506 (2004).